Lawrence Berkeley National Laboratory
LBL Publications

Title

Flexible Soft X-Ray Image Sensors based on Metal Halide Perovskites With High Quantum Efficiency

Permalink

https://escholarship.org/uc/item/8sw126ck

Authors

Tan, Pengju
Liu, Tianyu
Yang, Yuqian
et al.

Publication Date

2024-10-03

DOI

10.1002/adma.202407244

1 FRONT MATTER

2

3 **Title: Flexible Soft X-ray Image Sensors based on Metal Halide Perovskites with High**
4 **Quantum Efficiency**

5

6 **Authors**

7 Pengju Tan[1†], Tianyu Liu[1†], Yuqian Yang[1], Yuangan Chen[1], Yong Guan[2], Zidu Li[3],
8 Shunjie Yu[1], Xiaolong Zhao[1*], Yu Li[2], Honghe Ding[2], Xufei Wu[4], Zachary Fink[4], Shuang
9 Jia[5], Xiaohu Hou[1], Xuechen Jiao[2], Junfa Zhu[2], Fengjia Fan[3], Shangfeng Yang[5], Thomas P.
10 Russell[4,6], Xiaosong Liu[2*], Qin Hu[1*], Shibing Long[1]

11

12 **Affiliations**

13 [1]School of Microelectronics, University of Science and Technology of China, Hefei
14 230026, China

15 [2]National Synchrotron Radiation Laboratory, University of Science and Technology of
16 China, Hefei 230026, China\

17 [3]CAS Key Laboratory of Microscale Magnetic Resonance and School of Physical
18 Sciences, University of Science and Technology of China, Hefei, China

19 [4]Materials Sciences Division, Lawrence Berkeley National Laboratory, Berkeley,
20 California 94720, USA

21 [5]Key Laboratory of Precision and Intelligent Chemistry, Collaborative Innovation Center
22 of Chemistry for Energy Materials (iChEM), Department of Materials Science and
23 Engineering, University of Science and Technology of China, Hefei, 230026, China

24 6Polymer Science and Engineering Department, University of Massachusetts, Amherst,
25 MA 01003, USA

26

27 *e-mail: qinhu20@ustc.edu.cn; xlzhao77@ustc.edu.cn; xsliu19@ustc.edu.cn

28 [†]These authors contributed equally to this work.

29 **Abstract**

30 Soft X-ray imaging is a powerful tool to explore the structure of whole cells, probe large
31 volumes of material with nanometer resolution, and investigate the energetic phenomena
32 in the universe. Conventional soft X-ray image sensors are by and large silicon-based
33 charge coupled devices that suffer from low frame rates, complex fabrication processes,
34 required cooling below −60 ℃, and mechanical inflexibility. Here, we report a soft X-ray
35 photodiode based on a low-cost, solution-processed metal halide perovskite with
36 comparable performance to commercial Si-based devices. Design of the device structure
37 minimized the optical loss due to the shadowing of insensitive layers, while a
38 multidimensional perovskite heterojunction was gnerated to reduce the dark current
39 density and improve the quantum efficiency. A high responsivity of 0.161 A/W (@500
40 eV), an excellent quantum efficiency of 8×10^3 %, a low dark current density of 1.18×10^{-9}
41 A/cm², and a short response/decay time of 81/28 μs were achieved without cooling. Our
42 strategy promoted a record responsivity and quantum efficiency, several orders of
43 magnitude greater than the previously achieved and comparable to the commercial Si
44 based devices. Flexible and curved soft X-ray imaging arrays were fabricated based on

45　　this high-performance device structure, demonstrating stable soft X-ray response and
46　　sharp imaging capabilities. This work highlights the low-cost and efficient perovskite
47　　photodiode as a strong candidate for the next-generation soft X-ray imaging sensors.
48
49 **Teaser**
50　　Multidimensional perovskite heterojunction and delicate design of the device structure
51　　enhances the performance of perovskite soft X-ray photodiode.
52
53 **MAIN TEXT**
54
55 **Introduction**
56　　X-rays, a vital tool for scientific research and a multibillion-dollar industry, (*1*) can be
57　　divided into the hard and soft X-ray regimes depending on the photon energy. With
58　　photon energy greater than 10 keV, hard X-rays are penetrating and of great importance in
59　　medical diagnosis, security inspection, t name a few. (*2*) Soft X-rays have photon energies
60　　between several hundreds to thousands of electron-volts, are absorbed mmore readily and
61　　have a smaller absorption. Soft X-rays are mostly used in microscopy, spectroscopy, X-
62　　ray astronomy and lithography. (*3*) The "water window" spectral region lies between the
63　　carbon (284 eV) and oxygen (540 eV) K shell absorption edges. (*4*) Since water is nearly
64　　an order of magnitude more transparent than organics in this region, microscopic analysis
65　　of cells in their natural aqueous environment is possible. (*5*) Soft X-ray tomography inthe
66　　"water window" region allows for the 3D imaging of cellular ultrastructures with a
67　　resolution up to 25 nm, without the need for chemical or mechanical modification. (*6*)
68　　Apart from biological applications, soft X-ray microscopy can also probe large volumes of
69　　materials with nanometer resolution along with exquisite chemical, electronic and bond
70　　orientation contrast. (*7*) Soft X-ray telescopes onboard various satellites help collect key
71　　information about energetic phenomena in the universe. (*8*) For these applications, soft X-
72　　ray detectors and imaging sensors with high responsivity, low noise, low weight, and high
73　　cost-efficiency are highly desired. (*9*)

74　　Silicon-based charge coupled devices (CCDs) with direct detection mechanisms are
75　　commonly used for soft X-ray imaging at present, but they have many shortcomings,
76　　including costly fabrication processes, low frame rates, mechanical fragility, and cooling
77　　requirement from –60 ℃ to –130 ℃. (*10-12*) Recently, a number of novel materials, e.g.
78　　$CsPbBr_3$ perovskite nanocrystals, (*13*) $CrSiTe_3$ flake, (*14*) SnS nanosheets, (*9*) and
79　　$Cs_{0.1}FA_{0.9}PbI_3$ perovskite (FA: formamidine) films (*15*) have been explored for the direct
80　　detection of soft X-ray at room temperature. Among these materials, metal halide
81　　perovskites appear promising, since they have superior electrical and optoelectrictronic
82　　properties, such as large attenuation coefficients, long electron-hole diffusion lengths, high
83　　mobilities, high defect tolerances, and strong radiation tolerances. (*16*) In addition,
84　　perovskites can be produced as large-area films using low-cost solution processes,
85　　enabling the fabrication of cost-effective imaging sensor arrays, rather than individual
86　　photodetectors. While perovskite-based detectors in the hard X-ray region are widely
87　　reported to outperform commercial devices, (*17-19*) perovskite-based soft X-ray detectors
88　　are less explored. Liu et al. first introduced inkjet-printed $CsPbBr_3$ perovskite quantum
89　　dots for soft X-ray detection and successfully demonstrated direct detection of soft-X-ray-
90　　induced photocurrent with both rigid and flexible substrates. (*13*) The device showed a
91　　large dark current and low photon-to-dark current ratio, possibly due to the simple metal-

semiconductor-metal (MSM) structure adopted. In contrast, photodiode structures have low dark current, fast response speed, and low power consumption. (*19-22*) The n-i-p diode configuration in soft X-ray detectors was first used by Shabbir et al., and their $Cs_{0.1}FA_{0.9}PbI_3$ thin film based device achieved high performance across the soft and hard X-ray region. (*15*) Nevertheless, the soft X-ray responsivity of these reported devices was much lower than the theoretical limit of perovskite and also commercial Si-based devices. The severe optical loss and the photo-generated-carriers losses were the main reasons hindering the development of the perovskite-based soft X-ray photodiodes.

In this work, soft X-ray detectors based on low-cost, solution-processed $FAPbI_3$ perovskites are shown to have a performance that is comparable to commercial Si-based photodiodes. By designing the device structure to minimize the shadowing of insensitive layers and the generation of a multidimensional perovskite heterojunction to reduce charge carrier recombination, a high responsivity of 0.161 A/W (@500 eV) and an excellent quantum efficiency of 8×10^3 % were achieved. In addition, a low dark current density of 1.18×10^{-9} A/cm^2 at −2.5 mV and a short response/decay time of 81/28 μs were achieved. Based on this high-performance device structure, flexible and curved imaging arrays show stable soft X-ray response and excellent uniformity. Clear contrast images were achieved with a 10×10 crossbar array on glass. This work paves the way for perovskite photodiodes as practical, highly cost-effective and sensitive imager sensors for soft X-ray imaging systems.

Results

A Soft X-ray photodiode was built with a structure of indium tin oxide (ITO)/SnO_2/perovskite/poly[bis(4-phenyl) (2,4,6-trimethylphenyl)amine] (PTAA)/ Au (Fig. 1A). As different metal halide perovskite shows similar attenuation lengths in the soft X-ray region (fig. S1), we chose $FAPbI_3$ perovskite with well-developed fabrication, high thermodynamics stability and preferable photovoltaic properties for this work. To date, the most efficient perovskite solar cells usually use FA-rich perovskite as the light absorber layer, demonstrating the superiority of $FAPbI_3$ perovskite.(*23*) The attenuation lengths of soft X-ray in $FAPbI_3$ perovskite and Si are taken from the CXRO database and shown in Fig. 1B.(*24*) Si shows a steep increase of attenuation length at soft X-ray region from ~40 nm (@150 eV) to ~2.7 μm (@1000 eV). The small attenuation length at lower energy means that most absorption occurs in the defect-abundant surface region and the large attenuation length at higher energy reduces the attenuation efficiency of the active layer. These diminish diminish the performance of Si based soft X-ray detectors. However, $FAPbI_3$ perovskite shows stable attenuation lengths of serval hundreds of nanometers across the soft X-ray region, making it a suitable material for soft X-ray detection. The $FAPbI_3$ perovskite was obtained by a solution-based spin-coating process with a thickness of 750 nm, as shown in the cross-sectional scanning electron microscope (SEM) image in fig. S2. This thickness leads to an attenuation efficiency of ~90% at 500 eV.

The quality of the solution processed $FAPbI_3$ film was probed by multiple methods. Synchrotron-based grazing-incidence wide-angle X-ray scattering (GIWAXS) shows intense reflections at q ≈ 1, 1.4, 1.7, 2.0, and 2.2 $Å^{-1}$ (Fig. 1C and fig. S3), arising from the (100), (110), (111) , (200) and (210) planes of α-phase $FAPbI_3$. (*25*) No preferred orientation of the $FAPbI_3$ crystal was observed, suggesting the polycrystalline nature of

the sample. The top-view SEM image of the film shows an average grain size of ~1 μm (Fig. 1D). The absorption edge of the perovskite is located at 810 nm, consistent with the steady-state photoluminescence (PL) peak location (Fig. 1E). No sub-bandgap emission was observed in the PL spectra, confirming the high quality of the solution-processed perovskite film.

To estimate the functionality of the photodiode, the device response to visible light was first studied. As shown in the current–voltage (I-V) curves in Fig. 2A, the photodiode shows suppressed dark current under reverse bias. When 520 nm light (1.3 mW/cm^2) was turned on, typical photovoltaic behavior with high short-circuit current and large open-circuit voltage was observed, verifying a strong built-in electric field inside the photodiode. Unlike visible light, one main challenge for achieving high-performance detector in soft X-ray region is that soft X-ray shows small attenuation length in nearly all materials. (26) This leads to severe optical loss in insensitive layer on the active region in the detector and a special design of the device structure is needed. (26) Soft X-rays must be illuminated from the top side of our perovskite-based photodiode, since they penetrate the thick substrate. The top Au and PTAA layers are undesired "dead layers" that attenuate the light passing into perovskite. So, their thickness must be minimized while preserving the functionality of the photodiode (fig. S4). By exploring the device performance as a function of Au and PTAA layer thickness (Fig. 2B), thicknesses of 10 nm and 65 nm, respectively, were found to be optimal. For the fabrication of a high-performance soft X-ray photodiode, the modified structure ensures that the perovskite will absorb most of the incident soft X-rays and convert them into an electric signal (Fig. 2C). An absorption efficiency (defined as the ratio of the power absorbed by the active layer to the total incident power) greater than 50% was achieved across the soft X-ray region (fig. S5).

An obvious photoresponse is observed in our photodiode when illuminated by 500 eV soft X-rays with a photon flux of 6.92×10^{10} photons/s (Fig. 2D). A short-circuit current of 61.3 nA and an open-circuit voltage of 0.26 V were achieved. When working in the self-powered mode, meaing no applied external bias, the photodiode showed fast and stable response to the periodic exposure to 500 eV soft X-ray pulses (Fig. 2E). Under illumination, a 10^2-fold increase in the current was observed. For soft X-rays with photon energies from 300 to 800 eV, the device maintained significant response and good stability (fig. S6). To verify the response characteristics of the perovskite based soft X-ray photodiode more clearly, two figure-of-merits commonly used in commercial soft X-ray detectors were calculated. The responsivity (R) of the photodiode is defined as the photocurrent per incident radiation power: (27)

$$R = I_{\text{light}}/(\varphi \times E \times e)$$

Where I_{light} is the photocurrent, e is the charge of electron, φ represents the photon flux, and E denotes the photon energy of the incident soft X-ray. The quantum efficiency (QE) can be calculated as: (26)

$$QE = I_{\text{light}}/(\varphi \times e) = R \times E$$

The *QEs* of this perovskite-based soft X-ray photodiode at different photon energies are shown in Fig. 2F. The device is characterized with a *QE* and *R* of 5.53 and 11 mA/W, respectively, for 500 eV soft X-ray. The *QE* value exceeds 100% because the energetic soft X-ray photons can induce secondary electron cascades in semiconductors with multiple electrons being generated from one soft X-ray photon. (*1*) The theoretical *QE* of the perovskite semiconductor can be calculated as: (*28*)

$QE_{theoy} = E/W = E/(2E_g+1.43)$

Where *W* is the ionization energy of perovskite and E_g stands for the bandgap of the material. Given the bandgap of FAPbI$_3$ of 1.41 eV (fig. S7), QE_{theory} is 118 for this material for 500 eV soft X-rays. With an absorption efficiency of 64%, the theoretical *QE* and *R* limits of our device should be 76 and 0.15 A/W, respectively (fig. S8). The *QE* and *R* of our device achieved here are still far below the theoretical value sugesting a fast recombination of photogenerated carriers in the perovskite based soft X-ray photodiode.

To further improve the performance of the perovskite photodiode, a multidimensional perovskite heterojunction (MPH) was produced by epitaxial grow of 2D perovskites on the 3D FAPbI$_3$ surface. Significant performance improvement with lower dark current and better soft X-ray response was observed with the MPH (Fig. 3A). The dark current density of the device decreased by nearly one order of magnitude, reaching a value of 1.37×10^{-8} A/cm^2 at -0.5 V and 1.18×10^{-9} A/cm^2 at -2.5 mV. In addition, the photocurrent of the detector increased by nearly one order of magnitude. For the MPH device, a *QE* of 80 and a *R* of 0.161 A/W were achieved in the self-powered mode. These values are very close to the theoretical limits of the device, indicating a high charge collection efficiency for the MPH. This high charge collection efficiency can also be demonstrated by the spectral response of the MPH in the visible region, where a highest quantum efficiency >85% was achieved without the blocking of Au and PTAA layers (fig. S8). When exposed to intermittent illumination of 500 eV soft X-ray, the MPH photodiode maintained fast response and good reproducibility (Fig. 3B). Due to the lower dark current and higher photocurrent, the ratio between the photo and dark current reached 10^3 after the introduction of MPH. The rise/decay time of one photodetector is defined as the time delay between 10% and 90% of the steady photocurrent at the rising and falling edges. As shown in Fig. 3C, the response/decay time of the MPH device under 500 eV soft X-ray is ~10 ms. This value is not very precise, since the smallest time interval of the parameter analyzer used here is 10 ms. For reference, the device shows rise/decay of 81/28 μs with visible light when an oscilloscope with much higher time resolution was used (fig. S9). When working with different external biases and soft X-ray with different photon energies, the MPH device maintained a fast response and good stability (Figs. 3C and 3D). To further explore the stability of the device, fatigue tests were performed with the device being exposed for to soft X-rays for 1 sec with a 2 sec rest period between each exposure (Fig. 3F). After 130 cycles of exposure and a total absorption of ~9×10^{12} photons, which is far larger than the durability requirement of commercial soft X-ray imaging sensors (~10^{10} photons), (*10, 29*) the photo and dark current of the MPH device show negligible deterioration, refecting the good stability of our device.

To further explore the origin of the performance improvement after the introduction of the MPH, GIWAXS measurements were performed to probe the crystallization and

orientation of perovskite films. Additional reflections at q ≈ 0.25, 0.5, 0.75 $Å^{-1}$ are observed, arising from the (020), (040) and (060) planes, respectively, of $OA_2(FA)_{n-1}Pb_nI_{3n+1}$ 2D perovskite with n=2 (OA: n-Octylammonium) (Fig. 4A).[30, 31] These Bragg spots, concentrated along the q_z direction, suggest the 2D perovskite is oriented parallel to the substrate (fig. S11).[31] When different incidence angles were used, the 2D-perovskite-related peaks remain unchanged, while the 3D(100) signal shows a gradual increase with the increasing incidence angle (Fig. 4B). The peak area ratio between $(040)_{n=2}$ and 3D(100) decreases with an increase of the incidence angle and, therefore, penetration depth, indicating the surface-concentrated distribution of the 2D perovskite (Fig. 4C).[32, 33] An additional peak of n=2 phase 2D perovskite in 561 nm is observed in the UV-vis absorption spectrum of MPH sample, in line with the GIWAXS characterization results (fig. S12).[30] Given the results described above, the crystal structure of the MPH is shown in fig. S13. The surface chemistry of the perovskite film was investigated by X-ray photoelectron spectroscopy (XPS). Apart from the FA induced peak at 400.2 eV, the N 1s spectra of MPH sample show an additional peak at 401.8 eV, which is ascribed to the OA cation (fig. S14).[34] The C=O peak at 288.1 eV in C 1s spectra is significantly suppressed after the introduction of MPH (Fig. 4D), indicating the protection effect of the 2D perovskite against oxygen and moisture.[35] The time-resolved photoluminescence (TRPL) spectra of the MPH and control film on ITO/SnO_2 substrate are shown in Fig. 4E and the corresponding carrier lifetimes were determined from bi-exponential fitting. After the introduction of MPH, the average carrier lifetime of the perovskite increased from 6.8 ns to 35.0 ns, indicating a reduction of nonradiative recombination and defect states in the perovskite (Table S1).[33] This is also confirmed by the space-charge-limited current (SCLC) measurements (Fig. 4F), where the trap densities were found to be $8.3×10^{15}$ and $6.6×10^{15}$ for the control and MPH sample, respectively.[36]

Furthermore, we examined the photoexcitation and transport process of charge carriers inside the photodiode by transient absorption (TA) spectroscopy. A 2D pseudo-color plot of the TA spectroscopy of MPH film on glass substrate is shown in Fig. 4G. The blue region at 1.6 eV represents the photoinduced bleaching signal from band filling effect. [37, 38] The red region at 1.3-1.6 eV and the dark yellow region at 1.8-2.0 eV come from the bandgap renormalization effects and transient reflections, respectively. [39, 40] Normalized TA spectra at the early stage after photoexcitation shows a broadened high-energy tail (Fig. 4H and fig. S15), due to the non-thermalized hot carriers with high carrier temperature (T_c). [41, 42] The T_c can be extracted by fitting the high energy tail in the TA spectra to a Boltzmann distribution, as shown in Fig. 4I. [42] After generation from photoexcitation above the bandgap, hot carriers will release their excess kinetic energy by phonon emission and cooling down, leading to energy losses in the photoelectric conversion process. [43] The hot carrier cooling process can be fit with a bi-exponential function to determine the hot carrier lifetime (Table S2). [37, 41] After the introduction of MPH, the hot carrier lifetime shows a slight increase from 12.1 to 12.9 ps, showng that the MPH will not induce excess energy loss in this process. The charge transport process between PTAA and $FAPbI_3$ was examined using the long-term TA spectra of the stacks of these two layers (Fig. 4J and fig. S16). The evolution of photoinduced bleaching peak intensity (at 1.58 eV) with time is shown in Fig. 4K and fit with tri-exponential function. $τ_1$ is characteristic of the defect-mediated recombination in the perovskite. An increase in $τ_1$ from 315 to 1161 ps demonstrates the excellent passivation effect of MPH, in keeping the TRPL and SCLC measurements. [38] $τ_2$ is assigned to the hole injection from the

perovskite into PTAA, which also increases with the introduction of MPH (from 1.4 ns to 23 ns). (*44*) This may be due to the type-I band offset between 3D and 2D perovskite retarding hole transport. (*45*) We note that the wide-bandgap 2D perovskite can also increases the activation energy for thermal charge generation in the perovskite/PTAA interface, effectively loweing the dark current density of the device (Fig. 4L), as shown in Fig. 3A. (*45, 46*) The efficient passivation of defects guarantees that the carriers to go through the transport process without recombination, leading to higher quantum efficiency.(*47*)

For an image sensor, a curved surface is the preferred shape to match the curved focal plane of the lens system. (*48, 49*) For example, the advanced "lobster eye" soft X-ray telescope shows a focal plane with spherical shape (Fig. 5A).(*50*) Using traditional flat image sensor in such system will introduce vignetting problems and limit the field of view. (*48, 49*) Here the feasibility of fabricating curved imager sensors with the perovskite based soft X-ray photodiode was investigated. First, a perovskite photodiode on a flexible polyethylene naphthalate (PEN) substrate is shown with a stable soft X-ray response (Fig. 5B). Then, we fabricated 10×1 line arrays of the photodiode on the flexible substrate and bent them into a curved shape (Fig. 5C). Considering the practical difficulties of array test in a synchrotron radiation chamber and the performance similarity between the device under visible light and soft X-ray irradiation, 520 nm light was used for convenience to examine the performance of each pixel. Whether under dark or illumination conditions, the curved imaging array showed excellent uniformity and a good photo-to-dark current ratio. The image sensing functionality of the photodiode was verified with 10×10 imaging arrays on a glass substrate (Fig. 5D). The array shows good uniformity of dark and light current with no defective pixels (Fig. 5E). When a photomask with "USTC" was introduced, the array produced a sharp pattern with illumination (Fig. 5F). The performance of our perovskite based soft X-ray photodiode was compared to representative commercial and published soft X-ray detectors (Table 1). Our perovskite photodiode had an excellent comprehensive performance with low dark current, high responsivity and fast response. We note that the responsivity of our device was several orders of magnitude greater than that reported previousoy and comparable to commercial Si-based devices in the soft X-ray region.

Discussion

In summary, a high-performance soft X-ray detectors based on low-cost solution-processed perovskite photodiodes are demonstrated in this work. The design of the device was optimized to minimize the shadowing of "dead layers". With a multidimensional perovskite heterojunction, the dark current density of the device was reduced by nearly one order of magnitude and the response to soft X-rays increased by nearly one order of magnitude. A high responsivity of 0.161 A/W (@500 eV), an excellent quantum efficiency of $8×10^3$ %, a low dark current density of $1.18×10^{-9}$ A/cm^2, and short response/decay time of 81/28 μs were achieved. The responsivity and quantum efficiency of our device are several orders of magnitude greater than previously reported and comparable to commercial Si-based devices. Based on this high-performance device structure, flexible and curved soft X-ray imaging arrays were demonstrated with stable soft X-ray response and excellent uniformity. In addition, a 10×10 imaging array on a glass substrate showed good image sensing functionality. This work paves the way for perovskite photodiodes to serve as practical, highly cost-effective imaging sensors for soft X-ray system.

Materials and Methods

Materials

Lead iodide (PbI_2, 99.999%), formamidinium iodide (FAI, 98%), bis(trifluoromethane) sulfonimide lithium salt (Li-TFSI, 99.95%), n-Octylammonium iodide (OAI), anhydrous dimethylformamide (DMF, 99.8%), anhydrous dimethyl sulfoxide (DMSO, 99.9%), anhydrous isopropanol (IPA, 99.5%), anhydrous chlorobenzene (CB, 99.8%), 4-tert-butyl pyridine (TBP, 98%), anhydrous acetonitrile (ACN, 99.8%) were purchased from Sigma-Aldrich. Poly[bis(4-phenyl) (2,4,6-trimethylphenyl)amine] (PTAA, M_n = 6000-15000) was purchased from Xi'an Polymer Light Technology Corp (China). Tin (iv) oxide (SnO_2) colloid dispersion (in H_2O) and methylammonium chloride (MACl, 99.9%) were purchased from Advanced Election Technology Co., Ltd. All the chemicals are used as received without further purification. Indium Tin Oxide (ITO) glass (15 Ω/sq) and ITO on polyethylene naphthalate (PEN) substrate were purchased from Advanced Election Technology Co., Ltd.

Device Fabrication

Patterned ITO glass was cleaned in an ultrasonic bath with deionized water, detergent, deionized water, acetone, ethanol, and isopropanol for 15 min, respectively, followed by a UV-ozone treatment for 20 min. SnO_2 colloid precursor was diluted by deionized water (SnO_2 : H_2O = 1:4) and put in ultrasonic ice water bath for 25 min before use. Then the SnO_2 dispersion was spin coated onto the substrate at 3500 rpm for 25s and annealed in ambient air at 180 °C for 30 min. A UV-ozone treatment for 10 min was conducted before transferring the ITO/SnO_2 substrate to N_2-filled glove box. 1.8 M of PbI_2 and FAI in DMF:DMSO (6: 1) solvent with 35 mol% MACl was filtered and then deposited by spin coating at 1000 and 5000 rpm for 10 and 20 s, respectively. During the 5000-rpm spin coating program, 100 μL of CB was poured on the spinning substrate at the 15th second. Then the ITO/SnO_2/perovskite substrate was annealed in ambient air (35% humidity) at 150 °C for 10 min, followed by annealing in glove box at 100 °C for 10 min. For device with MPH, OAI solution (3.86 mg/mL, in IPA) was spin coated onto the perovskite surface at 3000 rpm for 30 s and annealed at 100 °C for 10 min. The hole transport material solution is consisted of 20 mg PTAA, 8 μL TBP, 15 μL Li-TFSI solution (170 mg/mL, in ACN), and 1 mL toluene. To get a PTAA layer with different thickness, the solution was diluted to various concentration before being deposited on the perovskite layer at 3000 rpm for 30 s. Finally, Au film with different thickness was thermally evaporated as top electrode. Typically, the active area of the individual device is 0.1071 cm^2.

For flexible device, PEN substrate with patterned ITO was cleaned in ultrasonic bath with ethanol for 5 min, followed by a UV-ozone treatment for 10 min. SnO_2 colloid precursor was diluted by deionized water (SnO_2 : H_2O = 1:1) and put in ultrasonic ice water bath for 25 min before use. Then the SnO_2 dispersion was spin coated onto the substrate at 5000 rpm for 60s and annealed in ambient air at 130 ºC for 20 min. Notably, the SnO_2 layer was spin-coated twice. The fabrication of other layers of the flexible photodiode was the same as the rigid one. As for the fabrication of imaging array, ITO glass was patterned through lithography and inductively coupled plasma etching to form bottom electrode line (ITO, 200 μm wide) before experiment. Special shadow mask was used to define top electrode

line (Au, 250 μm wide) vertical with the ITO line during the thermal evaporation. The pixel size is determined by the overlap of the ITO and the Au electrode. The other step of the fabrication was the same as the process to fabricate rigid individual device.

Film characterization:

Grazing-incidence wide-angle X-ray scattering (GIWAXS) was measured at beamline 7.3.3 at Advanced Light Source (ALS) at Lawrence Berkeley National Laboratory (LBNL, USA). All samples for GIWAXS were radiated at 10 keV X-ray with various incidence angle. The surface morphology and cross-sectional image of the perovskite was investigated by scanning electron microscope (SEM, Hitachi SU8220). The absorption spectrum of perovskite was estimated by UV-vis-NIF spectrometer (Shimadze 3700 DUV). The steady-state and time-resolved photoluminescence (PL and TRPL) was measured using a Horiba Fluorolog-3 and DeltaFlex system, respectively. A PHI 5000 VersaProbe III system with a monochromatic Al Kα X-ray source was used to perform X-ray photoelectron spectroscopy (XPS) test. The thickness of the PTAA layer was estimated by a profiler (Dektak XT). The transient absorption measurements are conducted with fundamental laser (10 kHz) generated by Yb:KGW regenerative amplifier. Optical parametric amplifier used to produce 3.1-eV photoexcitation pulse (with an intensity of 3.2 mW and a pulse duration ~250 fs). Optical bench directed both lasers, with fundamental laser focused into sapphire crystal to generate white light probe. Photoexcitation pulse frequency reduced to 5 kHz using chopper. Both lasers focused onto sample in 1-mm cuvette, probe signal detected by CCD.

Device performance characterization

The device performance under soft X-ray was tested at beamline BL07W of national synchrotron radiation laboratory (NSRL, China). A standard AXUV-100G photodiode was used to calibrate the photon flux before test. During the test, the electrical properties of the device were examined by a Keithley 4200 Parameter Analyzer. To record the device performance under 520 nm light (for both individual device and imaging array), a mLaser laser source, a Keithley 6482 Picoammeter, and a probe station in a N_2-filled glovebox were adopted. For imaging array, the current was recorded pixel by pixel, so as the light illumination. The quantum efficiency of the device across the visible light region was measured on a xenon lamp-based system (Newport TLS260-300X, USA). The transient photocurrent (TPC) under 520 nm light was measured using a waveform generator (Rigol DG822), a pre-amplifier (Stanford Research Systems SR570), and a digital oscilloscope (PicoScope 4262).

Soft X-ray intensity distribution simulation

The distribution of the Soft X-ray intensity throughout the Si, $FAPbI_3$, and photodiode was calculated following the Beer-Lambert Law, which can be expressed as:

$$I = I_0 \exp \left(\frac{-t}{t_0(E)} \right)$$

Where I is the soft X-ray intensity through material of thickness t, I_0 is the incident intensity and the $t_0(E)$ stand for the attenuation length of soft X-ray in this material, which was taken from the CXRO database.

Space-charge-limited current measurements

The SCLC measurements were performed on electron-only device with structure of ITO/SnO$_2$/perovskite (with or without MPH)/C$_{60}$/BCP/Ag. The defect density is calculated as:

$$n_t = \frac{2\varepsilon\varepsilon_0 V_{TFL}}{eL^2}$$

Where ε is the relative permittivity of FAPbI$_3$ perovskite (taken as 46.9 here), ε_0 is the vacuum permittivity, L is the thickness of the FAPbI$_3$ film (750 nm), e is the elementary charge, and V_{TFL} is the trap-filled limit voltage.

Fitting models for the decay process

The TRPL, hot carrier cooling process, and bleach peak intensity decay process is fitted with biexponential or triexponential equation, which can be express as:

$$I = I_0 + \sum_{i=1}^{n} A_i \exp\left(\frac{-t}{\tau_i}\right)$$

Where t is the time, τ_i and A_i is the life time and amplitude of the process, respectively. For biexponential equation, n=2; while for triexponential equation, n=3. The average lifetime (τ_{ave}) is obtained by:

$$\tau_{ave} = \frac{\sum_{i=1}^{n} A_i \tau_i^2}{\sum_{i=1}^{n} A_i \tau_i}$$

References

1. H. Wu, Y. Ge, G. Niu, J. Tang, Metal halide perovskites for X-ray detection and imaging. *Matter* **4**, 144-163 (2021).
2. P. J. Withers *et al.*, X-ray computed tomography. *Nat. Rev. Methods Primers* **1**, 18 (2021).
3. S. Suckewer, C. H. Skinner, Soft X-ray lasers and their applications. *Science* **247**, 1553-1557 (1990).
4. J. Kirz, C. Jacobsen, M. Howells, Soft X-ray microscopes and their biological applications. *Quart. Rev. Biophys.* **28**, 33-130 (1995).
5. M. C. A. Dyhr *et al.*, 3D surface reconstruction of cellular cryo-soft X-ray microscopy tomograms using semisupervised deep learning. *Proc. Natl. Acad. Sci. U. S. A.* **120**, e2209938120 (2023).
6. M. Harkiolaki *et al.*, Cryo-soft X-ray tomography: using soft X-rays to explore the ultrastructure of whole cells. *Emerg. Top. Life Sci.* **2**, 81-92 (2018).
7. D. A. Shapiro *et al.*, Chemical composition mapping with nanometre resolution by soft X-ray microscopy. *Nat. Photonics* **8**, 765-769 (2014).
8. N. Ogino *et al.*, Performance verification of next-generation Si CMOS soft X-ray detector for space applications. *Nucl. Instrum. Methods Phys. Res. A* **987**, 164843 (2021).
9. B. Shabbir *et al.*, Soft X-ray detectors based on SnS nanosheets for the water window region. *Adv. Funct. Mater.* **32**, 2105038 (2021).

442 10. K. Desjardins *et al.*, Backside-illuminated scientific CMOS detector for soft X-ray
443   resonant scattering and ptychography. *J. Synchrotron Radiat.* **27**, 1577-1589 (2020).
444 11. J. Heymes *et al.*, Characterisation of a soft X-ray optimised CMOS image sensor. *J.
445   Instrum.* **17**, P05003 (2022).
446 12. S. Tammes *et al.*, Soft x-ray detection for small satellites with a commercial CMOS sensor
447   at room temperature. *J.Astron. Telesc. Instrum.Syst.* **6**, 046004 (2020).
448 13. J. Liu *et al.*, Flexible, printable soft-X-ray detectors based on all-inorganic perovskite
449   quantum dots. *Adv. Mater.* **31**, 1901644 (2019).
450 14. Y. Li *et al.*, High performance broadband photo and soft X-ray detectors based on two
451   dimensional $CrSiTe_3$. *J. Mater. Chem. C* **8**, 6659-6666 (2020).
452 15. B. Shabbir *et al.*, Printable perovskite diodes for broad-spectrum multienergy X-ray
453   detection. *Adv. Mater.* **35**, 2210068 (2023).
454 16. Y. Wu, J. Feng, Z. Yang, Y. Liu, S. F. Liu, Halide perovskite: a promising candidate for
455   next-generation X-ray detectors. *Adv. Sci.* **10**, e2205536 (2022).
456 17. H. Tsai *et al.*, A sensitive and robust thin-film X-ray detector using 2D layered perovskite
457   diodes. *Sci. Adv.* **6**, eaay0815 (2020).
458 18. Y. C. Kim *et al.*, Printable organometallic perovskite enables large-area, low-dose X-ray
459   imaging. *Nature* **550**, 87-91 (2017).
460 19. K. Sakhatskyi *et al.*, Stable perovskite single-crystal X-ray imaging detectors with single-
461   photon sensitivity. *Nat. Photonics* **17**, 510 (2023).
462 20. L. Li *et al.*, Recent advances in perovskite photodetectors for image sensing. *Small* **17**,
463   e2005606 (2021).
464 21. Y. Zhou *et al.*, Self-powered perovskite photon-counting detectors. *Nature* **616**, 712-718
465   (2023).
466 22. A. J. J. M. van Breemen *et al.*, A thin and flexible scanner for fingerprints and documents
467   based on metal halide perovskites. *Nat. Electron.* **4**, 818 (2021).
468 23. Z. Liu *et al.*, Efficient and stable FA-rich perovskite photovoltaics: from material
469   properties to device optimization. *Adv. Energy Mater.* **12**, 2200111 (2022).
470 24. B. L. Henke, E. M. Gullikson, J. C. Davis, X-Ray interactions: photoabsorption,
471   scattering, transmission, and reflection at E = 50-30,000 eV, Z = 1-92. *Atom. Data Nucl.
472   Data Tables* **54**, 181-342 (1993).
473 25. W. Peng *et al.*, Reducing nonradiative recombination in perovskite solar cells with a
474   porous insulator contact. *Science* **379**, 683-690 (2023).
475 26. M. Krumrey *et al.*, Schottky type photodiodes as detectors in the VUV and soft X-ray
476   range. *Appl. Opt.* **27**, 4336-4341 (1988).
477 27. D. Skroblin *et al.*, Vacuum-compatible photon-counting hybrid pixel detector for wide-
478   angle X-ray scattering, X-ray diffraction, and X-ray reflectometry in the tender X-ray
479   range. *Rev. Sci. Instrum.* **91**, 023102 (2020).
480 28. R. Devanathan, L. R. Corrales, F. Gao, W. J. Weber, Signal variance in gamma-ray
481   detectors—A review. *Nuclear Inst. and Methods in Physics Research* **565**, 637-649
482   (2006).
483 29. T. Harada *et al.*, High-exposure-durability, high-quantum-efficiency (>90%) backside-
484   illuminated soft-X-ray CMOS sensor. *Appl. Phys. Express* **13**, 016502 (2019).
485 30. L. Shen *et al.*, Ion-diffusion management enables all-interface defect passivation of
486   perovskite solar cells. *Adv. Mater.* **35**, e2301624 (2023).
487 31. F. Li *et al.*, Effects of alkyl chain length on crystal growth and oxidation process of two-
488   dimensional tin halide perovskites. *ACS Energy Lett.* **5**, 1422-1429 (2020).

32. L. Zhao *et al.*, Chemical polishing of perovskite surface enhances photovoltaic performances. *J. Am. Chem. Soc.* **144**, 1700-1708 (2022).

33. Y. Zhang *et al.*, Mechanochemistry advances high-performance perovskite solar cells. *Adv. Mater.* **34**, e2107420 (2022).

34. S. Ding *et al.*, In situ bonding regulation of surface ligands for efficient and stable FAPbI$_3$ quantum dot solar cells. *Adv. Sci.* **9**, e2204476 (2022).

35. Q. Jiang *et al.*, Surface passivation of perovskite film for efficient solar cells. *Nat. Photonics* **13**, 460-466 (2019).

36. J. Park *et al.*, Controlled growth of perovskite layers with volatile alkylammonium chlorides. *Nature* **616**, 724-730 (2023).

37. G. Yang *et al.*, Study on carrier dynamics of perovskite solar cells via transient absorption. *J. Alloys Compd.* **952**, 170051 (2023).

38. M. Singh *et al.*, Unveiling ultrafast carrier extraction in highly efficient 2D/3D bilayer perovskite solar cells. *ACS Photonics* **9**, 3584-3591 (2022).

39. J. Liu, J. Leng, S. Wang, J. Zhang, S. Jin, Artifacts in transient absorption measurements of perovskite films induced by transient reflection from morphological microstructures. *J. Phys. Chem. Lett.* **10**, 97-101 (2019).

40. S. Narra *et al.*, Femtosecond transient absorption spectra and dynamics of carrier relaxation of tin perovskites in the absence and presence of additives. *J. Phys. Chem. Lett.* **11**, 5699-5704 (2020).

41. L. Zhu *et al.*, Slowing the hot-carrier cooling by an organic small molecule in perovskite solar cells. *EcoMat* **5**, e12313 (2022).

42. M. B. Price *et al.*, Hot-carrier cooling and photoinduced refractive index changes in organic-inorganic lead halide perovskites. *Nat. Commun.* **6**, 8420 (2015).

43. Z. Guo *et al.*, Long-range hot-carrier transport in hybrid perovskites visualized by ultrafast microscopy. *Science* **356**, 59 (2017).

44. L. Wang, C. McCleese, A. Kovalsky, Y. Zhao, C. Burda, Femtosecond time-resolved transient absorption spectroscopy of CH$_3$NH$_3$PbI$_3$ perovskite films: evidence for passivation effect of PbI$_2$. *J. Am. Chem. Soc.* **136**, 12205-12208 (2014).

45. R. Ollearo *et al.*, Multidimensional perovskites for high detectivity photodiodes. *Adv. Mater.* **34**, e2205261 (2022).

46. R. Ollearo *et al.*, Ultralow dark current in near-infrared perovskite photodiodes by reducing charge injection and interfacial charge generation. *Nat. Commun.* **12**, 7277 (2021).

47. G. Wu *et al.*, Surface passivation using 2D perovskites toward efficient and stable perovskite solar cells. *Adv. Mater.* **34**, e2105635 (2022).

48. A. J. J. M. van Breemen *et al.*, Curved digital X-ray detectors. *npj Flexible Electron.* **4**, 22 (2020).

49. W. Gao, Z. Xu, X. Han, C. Pan, Recent advances in curved image sensor arrays for bioinspired vision system. *Nano Today* **42**, 101366 (2022).

50. M. Ouyang *et al.*, Comprehensive understanding of the focal property of lobster-eye optics. *Appl. Opt.* **59**, 4263-4270 (2020).

Author contributions: Q.H. conceived the idea. Q.H., X.Z and X.L. directed and supervised the project. Q.H. and P.T. designed all the experiments. P.T. and T. L. fabricated and characterized the photodiodes, prepared the samples for characterizations. Y.Y and Y.C. supported the device fabrication. Y.G., S.Y. helped to characterize the soft X-ray response. Z. L. conduct the TAS experiments. X.W. and Z.F. conducted the GIWAX measurements. Y.L., H.D., X.J., X. H., S. J., J.Z., F. F., S.Y., T.P.R. and S.L. gave suggestions and comments. P.T. and T.L. wrote the manuscript. Q.H., X.Z., X. L. and Y.L. revised the paper. All the authors discussed the results and commented on the paper.
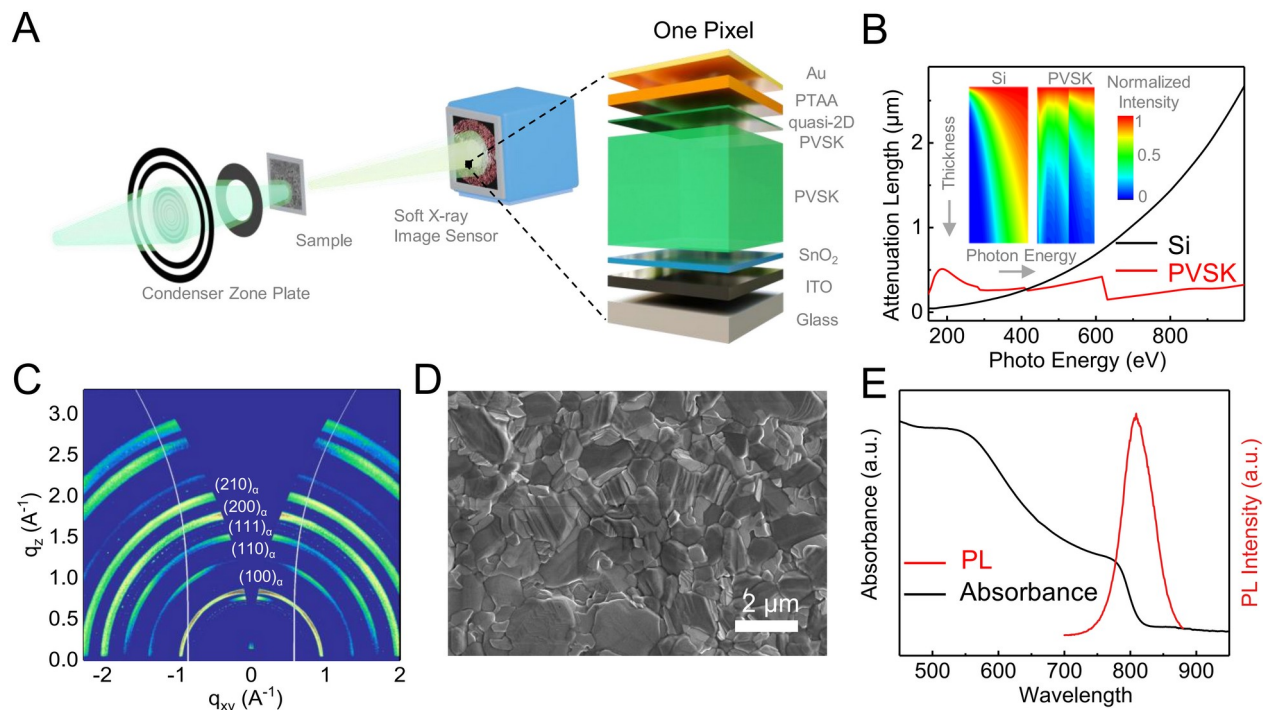
Competing interests: The authors declare no competing financial interests.

Data and materials availability: Supporting information was available in the online version of the paper. Correspondence and requests for materials should be addressed to Q.H., X.Z. and X. L..

Figures and Tables

569

570

571 **Fig. 1. Device structure and material characterization.** (**A**) Schematic diagram of one soft X-
572 ray microscopy system with perovskite (PVSK) photodiode array as image sensor. (**B**)
573 Comparison of attenuation length of soft X-ray in Si and FAPbI$_3$, while inset depicts the variation
574 of soft X-ray intensity throughout these two materials with the same thickness (750 nm). FAPbI$_3$
575 shows more uniform attenuation length and light intensity distribution across the soft X-ray region.
576 (**C**) The 2D GIWAXS pattern of FAPbI$_3$ film at beam incidence angle of 0.5°. (**D**) Top-view SEM
577 image of the FAPbI$_3$ perovskite film. (**E**) Absorption and PL spectra of FAPbI$_3$ perovskite.
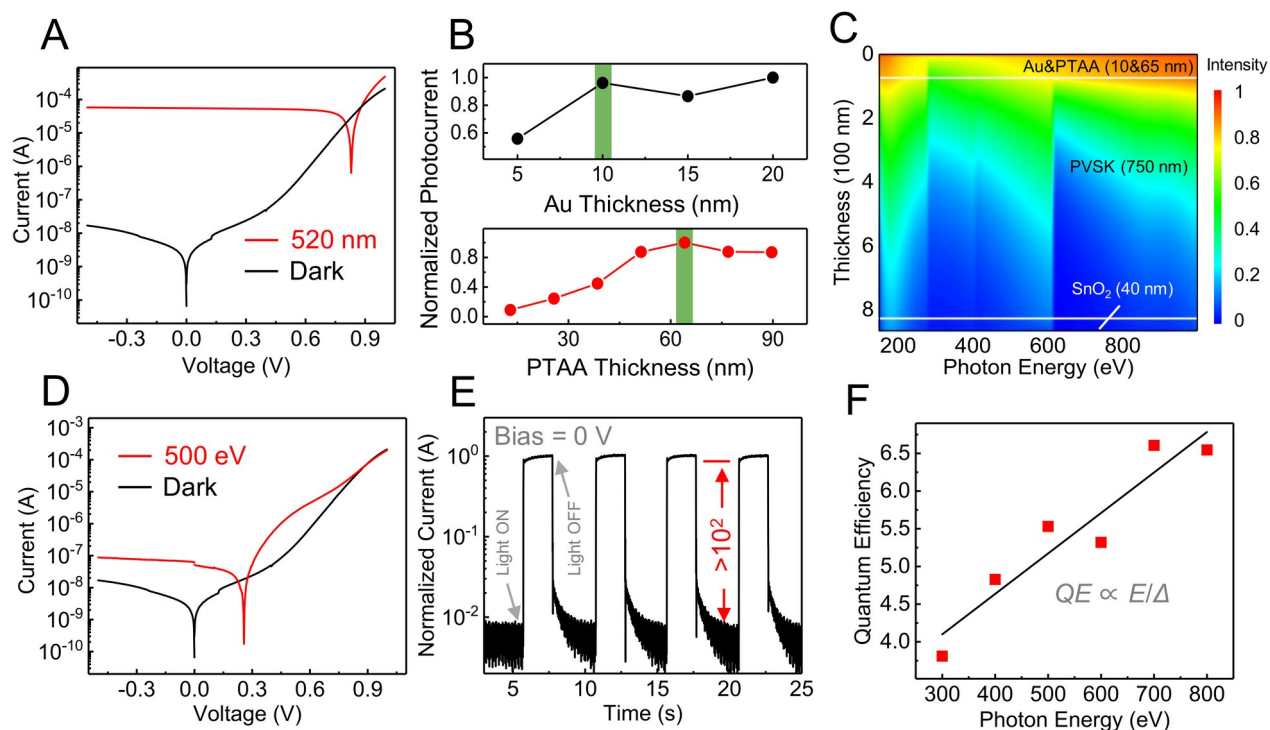
579

Fig. 2. Performance of the control device. (**A**) Photovoltaic behavior of the perovskite photodiode under 520 nm light (1.3 mW/cm^2). (**B**) Dependence of photocurrent (under 520 nm light) of the device on the thickness of Au and PTAA layer, respectively. The optimal thickness is 10 and 68 nm for Au and PTAA, respectively. (**C**) Distribution of soft X-ray intensity throughout the photodiode with adjusted structure. (**D**) I-V curve of the perovskite photodiode in the dark and under 500 eV soft X-ray with photo flux of 6.92×10^{10} photons/s. (**E**) Light switching response of the perovskite photodiode at 0 V under 500 eV soft X-ray. (**F**) The linear relationship between device quantum efficiency (*QE*) and photon energy (*E*), which is in line with the given formula.
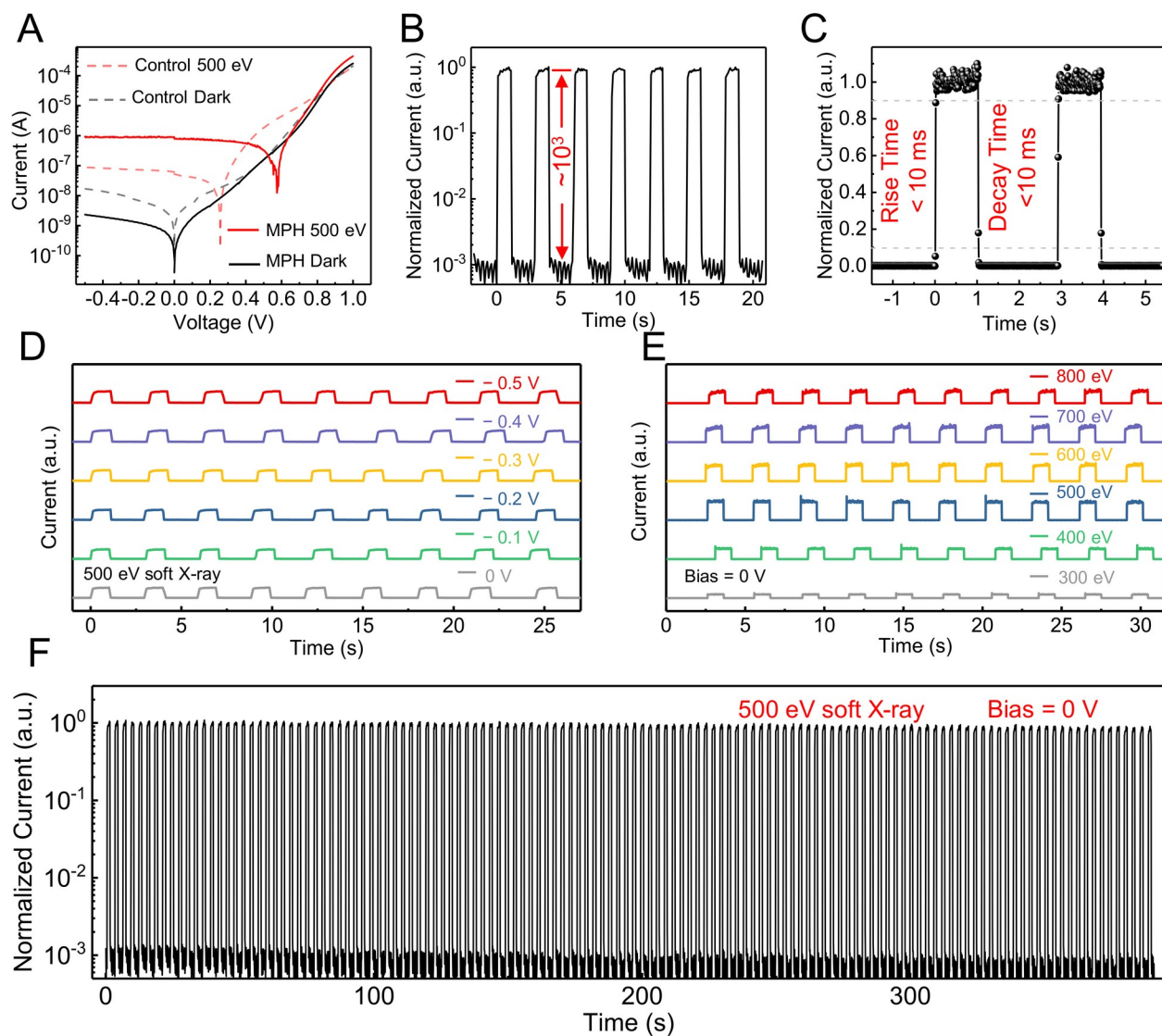
Fig. 3. Performance of the multidimensional perovskite heterojunction (MPH) device. (**A**) Comparison of I-V curves of the perovskite photodiode with and without MPH (in the dark and under 500 eV soft X-ray). (**B**) Response of the MPH device to intermittent illumination of 500 eV soft X-ray. (**C**) Close-up view of the typical response period of the device in linear scale, which shows rise and decay time smaller than 10 ms. (**D, E**) Light switching response of the photodiode with MPH at various voltages and different photon energy, respectively. (**F**) Multi-cycle time-dependent response of the MPH device under the excitation of 500 eV soft X-ray at zero bias.
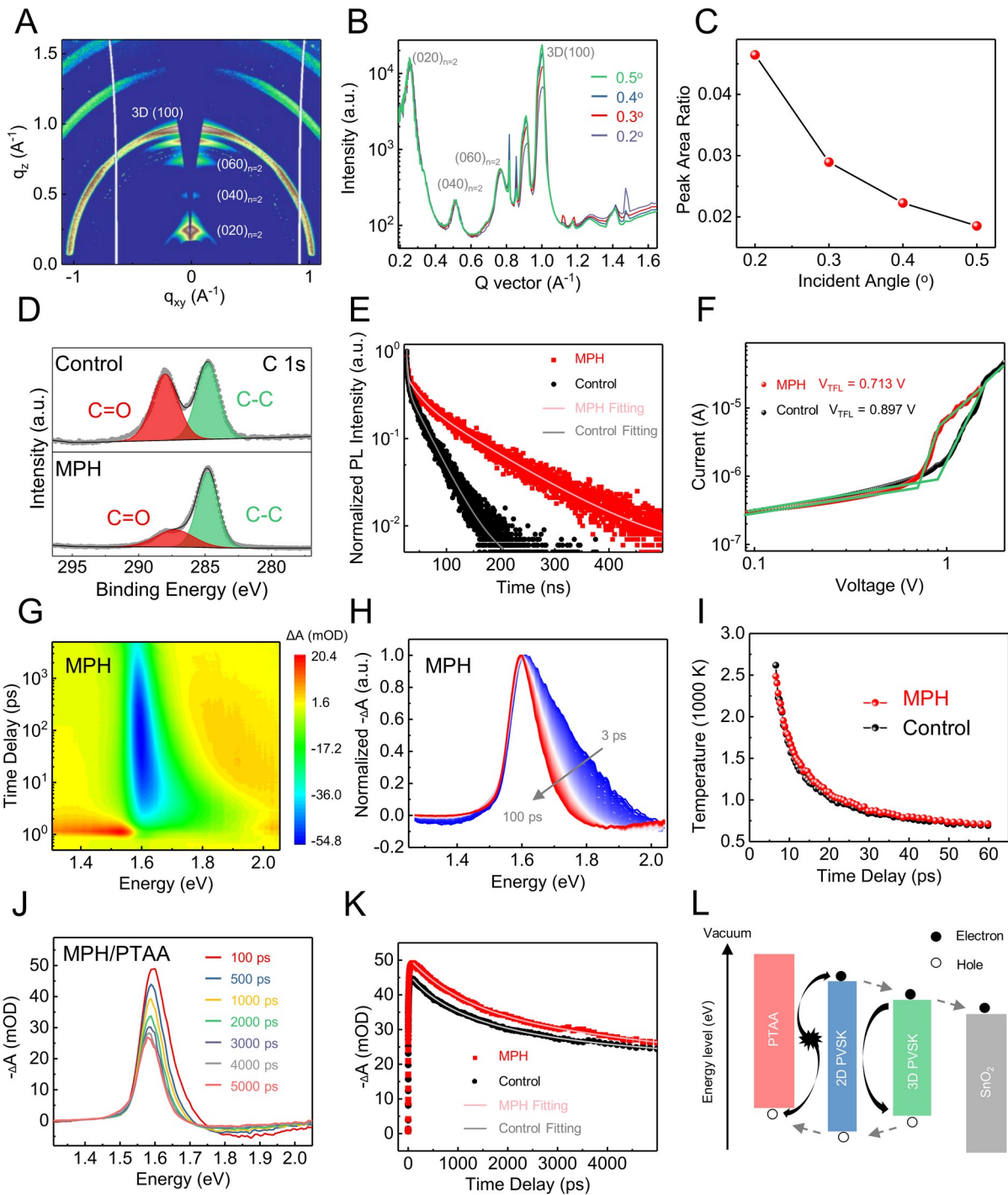
Fig. 4. Characterization of the effect of MPH on the device. (**A**) 2D pattern of the GIWAXS of the multidimensional heterojunction, recorded under an incidence angle of $0.5°$. (**B**) Integrated line file GIWAXS of the MPH film with various incidence angle. (**C**) The area ratio of $(040)_{n=2}$ peak to 3D(100) peak as a function of incidence angle. (**D**) XPS C 1s core level spectra of $FAPbI_3$ perovskite with and without MPH, respectively. (**E**) TRPL decays of the control and MPH film on ITO/SnO_2 substrate. (**F**) The dark I-V characteristics of electron-only device with structure of ITO/ SnO_2/perovskite (with or without MPH)/C_{60}/BCP/Ag, and V_{TFL} stands for the trap-filled limit voltage. (**G**) Color plot of the transient absorption (TA) spectra of the MPH film on glass substrate. (**H**) Normalized TA spectra of the MPH sample from 3 to 100 ps. (**I**) The hot carrier temperature as a function of delay time. (**J**) Evolution of the TA spectra of the MPH/PTAA film probed at

varied delays as indicated. (**K**) Transient band edge bleach kinetics of the perovskite/PTAA film with and without MPH. (**L**) Schematic band diagram of the photodiode with MPH.
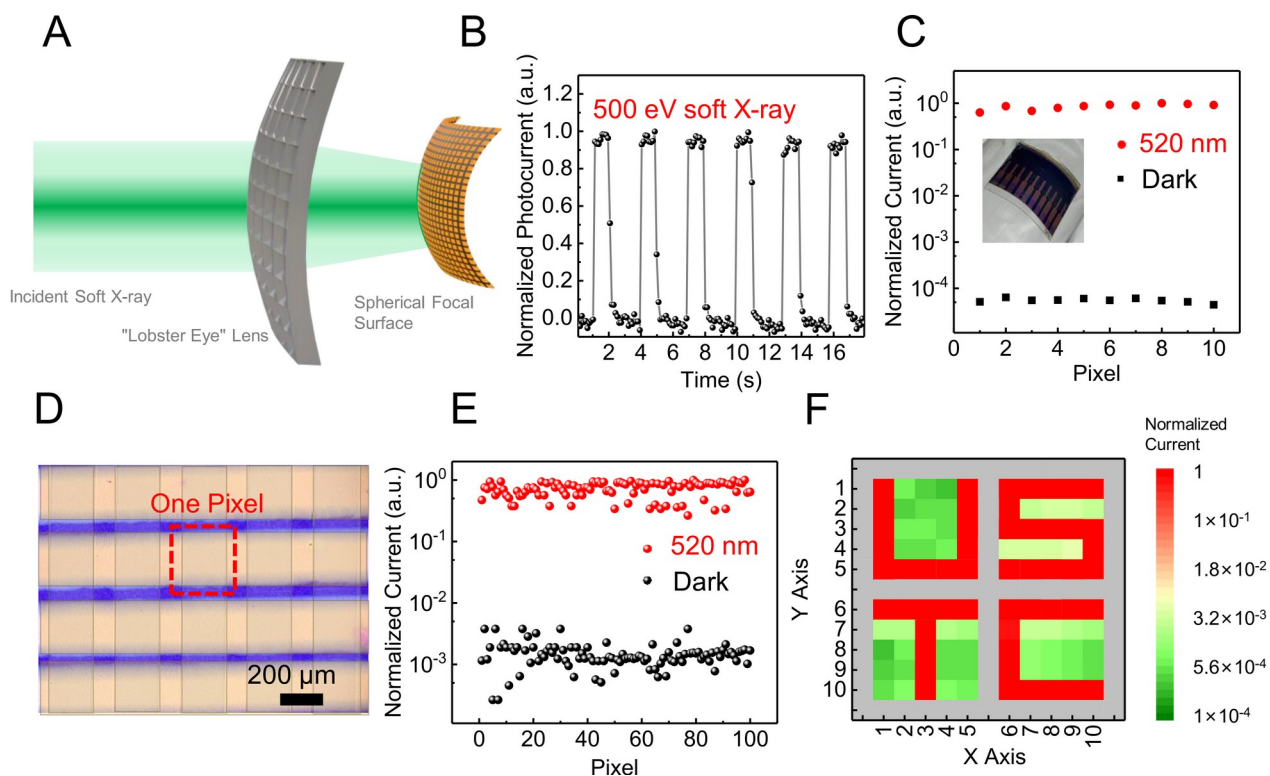
Fig. 5. Demonstration of curved image sensor. (**A**) Schematic diagram of the "lobster eye" soft X-ray imaging system. (**B**) Light switching response under 500 eV soft X-ray of the flexible perovskite photodiode on PEN substrate at self-powered mode. (**C**) The dark and light current of each pixel of a flexible 10×1 line array under a bending radius of 1.4 cm (corresponding to a bending angle of ~60°). Inset shows the curved array. (**D**) Optical image of parts of the 10×10 crossbar array with one pixel as 200×250 μm^2. (**E**) Dark and light current mapping of the photodiode array. (**F**) Imaging results of the imaging array under photomask. The image has been rearranged for clarification. Focusing light spot was used during the test to evade crosstalk issue.

Table 1. Comprehensive comparison of the perovskite based soft X-ray photodiode (with MPH) with other soft X-ray detectors from market and literature. The responsivity and quantum efficiency of our device are several orders of magnitude larger than the previous reports and comparable to commercial Si based device.

Material	structure	Dark current density (nA/cm²)	Sensitivity (µC/Gy/cm²)	Responsivity (A/W)	Quantum Efficiency (%)	Decay Time (µs)	Temperature (°C)	Ref
Si	PN diode	0.736 (@10 mV)	--	0.268 (@500 eV)	1.37×10^4 (@500 eV)	10	RT	A
Si	CCD image sensor	--	--	0.235 (@500 eV)	1.2×10^4 (@500 eV)	--	−70	B
Si	Cmos image sensor	--	--	0.155 (@500 eV)	7.9×10^3 (@500 eV)	< 21	−20	C
SnS	MSM	$\sim6\times10^4$ (@1 V)	1.15×10^4 (@600 eV)	$\sim2\times10^{-5}$ (@600 eV)	~1.2 (@600 eV)	2×10^3	RT	(9)
$CsPbBr_3$ Perovskite	MSM	$\sim1\times10^4$ (@0.1 V)	1450	--	--	2.7×10^4	RT	(13)
$CrSiTe_3$	MSM	$\sim8\times10^7$ (@1 V)	463 (@800 eV)	--	--	1.06×10^5	RT	(14)
$Cs_{0.1}FA_{0.9}PbI_3$ Perovskite	diode	~7 (@1 mV)	5×10^3 (@700 eV)	$\sim5\times10^{-3}$ (@700 eV)	$\sim3.5\times10^2$ (@700 eV)	3×10^3	RT	(15)
$FAPbI_3$ Perovskite	**diode**	**1.18 (@2.5 mV)**	**--**	**0.161 (@500 eV)**	**8×10^3 (@500 eV)**	**28**	**RT**	**This Work**

--: not mentioned or ambiguous in corresponding reference. RT: room temperature

A: AXUV100G from Opto Diode Corp.; B: PIXIS-XO: 1024B from Princeton Instruments Inc.; C: GSENSE400BSI from Gpixel

Supplementary Materials

Supporting information for this article is available online.